

# Structural symmetry and membrane curvature sensing

Federico Elías-Wolff\*

*Department of Biochemistry and Biophysics, Stockholm University, Sweden*

Alexander Lyubartsev<sup>†</sup> and Erik G. Brandt<sup>‡</sup>

*Department of Materials and Environmental Chemistry, Stockholm University, Sweden*

Martin Lindén<sup>§</sup>

*Department of Cell and Molecular Biology, Uppsala University, Sweden*

*Present address: Scania CV AB, Södertälje, Sweden*

(Dated: March 10, 2024)

Symmetry is closely intertwined with the function, genetics, and chemical properties of multi-protein complexes. Here, we explore the relation between structural symmetry and the ability of membrane proteins to sense and induce membrane curvature, which is a key factor for modulating the shape and organization of cell membranes. Using coarse-grained simulations and elasticity theory, we show that the potential for direction-dependent membrane curvature sensing is limited to asymmetric proteins, dimers, and tetramers, and argue that one should expect this anisotropy to be strongest for dimers. Odd and higher-order symmetries strongly suppress directional curvature sensing. This classification gives a new perspective on the structure-function relation for membrane proteins, and simplifies the task of translating between molecular sensing mechanisms and their large-scale cellular consequences.

Cell membranes are subject to large and dynamic deformations, mainly driven by the ability of membrane proteins to sense, influence, and respond to local membrane curvature [1–4]. There is a growing list of molecular mechanisms of curvature sensing, including insertion of amphipathic peptides into the lipid headgroup region (wedge mechanism) [5, 6], curved protein-lipid interfaces of peripheral membrane proteins such as BAR domains (scaffold mechanism) [7], and non-cylindrical transmembrane domains of integral membrane proteins [4, 8]. These mechanisms clearly depend on the protein structure, and many membrane proteins are highly symmetric [9], but the role of protein structural symmetry for curvature sensing has, to the best of our knowledge, not been systematically explored. Here, we set out to do that.

The main mechanism behind protein structural symmetry is homo-oligomerization, where multiple identical subunits form a functional protein unit. Since reflection and inversion symmetries are ruled out by the chirality of the  $\alpha$ -carbon in polypeptide chains, and biological membranes usually have asymmetric leaflets (different inside and outside), by far the most common symmetries for membrane proteins are cyclic groups that describe finite-size rotations around the membrane normal [9].

While many curvature sensing mechanisms depend on molecular details, their biological consequences in terms of membrane shape and organization typically play out on the much larger length scales of organelles (10 nm and up) or whole cells [1–3]. Bridging this gap of scales is

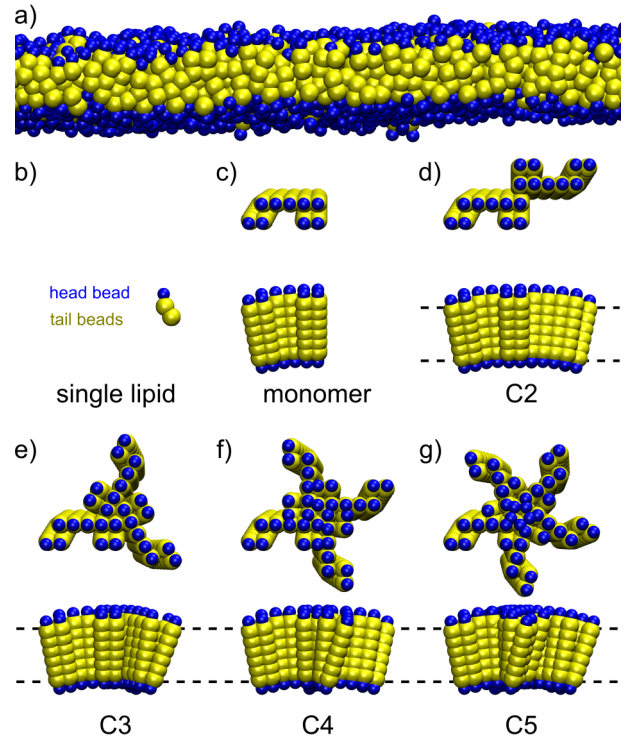


FIG. 1. Coarse-grained lipids and proteins. (a) Side-view of a flat patch of a coarse-grained fluid membrane, which in our parameter regime has a thickness of  $\sim 5\sigma$  [10]. (b) Single 3-bead lipid with one head bead (blue) and two tail beads (yellow). (c) Protein monomer. (d-g) Top- and side views of protein multimers with 2- to 5-fold cyclic symmetry.

\* federico.elias.wolff@dbb.su.se

<sup>†</sup> alexander.lyubartsev@mmk.su.se

<sup>‡</sup> erik.brandt@mmk.su.se

<sup>§</sup> bmelinden@gmail.com

a key challenge in understanding the biological functions of membrane curvature sensing.

Simplified theoretical models, provide a natural route

to this end. Membranes are then modeled as thin elastic sheets decorated with proteins whose binding energies are functions of the local membrane curvature. Since proteins have complex shapes, curvature sensing will be coupled to the binding orientation as well as the protein position [11]. This is best described by a protein binding energy that depends on the local curvature tensor in the protein's frame of reference [11–17]. Numerical studies indicate that such anisotropic curvature-sensors are capable of complex, large-scale membrane remodeling [13]. Here, we explore how these types of interactions are restricted by protein structural symmetry, and argue that these restrictions have biological implications: for membrane proteins, different symmetries are suited for different functions.

We use a coarse-grained implicit-solvent model of membranes in the fluid phase to study generic effects of cyclic symmetry on curvature sensing. Single lipids are represented by one head bead and two tail beads [18] (Fig. 1a,b). We construct an asymmetric monomer with a slight wedge-shaped transmembrane region from tail beads sandwiched between head beads (Fig. 1c), and assemble cyclic multimers by in-plane rotations (Fig. 1d-g). The model proteins are stabilized by a network of elastic springs. The trimer in this family has a preferred curvature of about  $0.035\sigma^{-1}$  in our parameter regime [19] ( $\sigma \approx 1\text{nm}$  being the coarse-grained length unit [10]). For further details, see Supplementary methods.

The cyclic symmetry of the protein complex couples directly to its in-plane orientation. We simulated proteins on a cylindrical bilayer and measured the in-plane orientation (Fig. 2). The curvature is uniform in cylindrical geometry, so that the curvature tensor seen by the protein is determined completely by the protein orientation, and we do not need to constrain or keep track of the protein position.

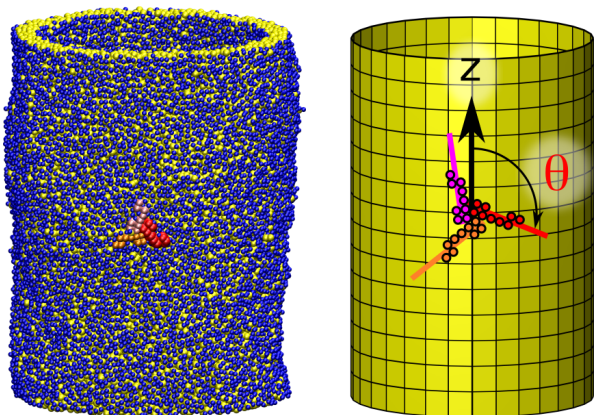


FIG. 2. Protein orientation on a cylinder. (Left) snapshot of a trimer simulation, with the monomers colored red, orange, and pink. (Right) Analysis sketch with in-plane angle  $\theta$  for the first monomer.

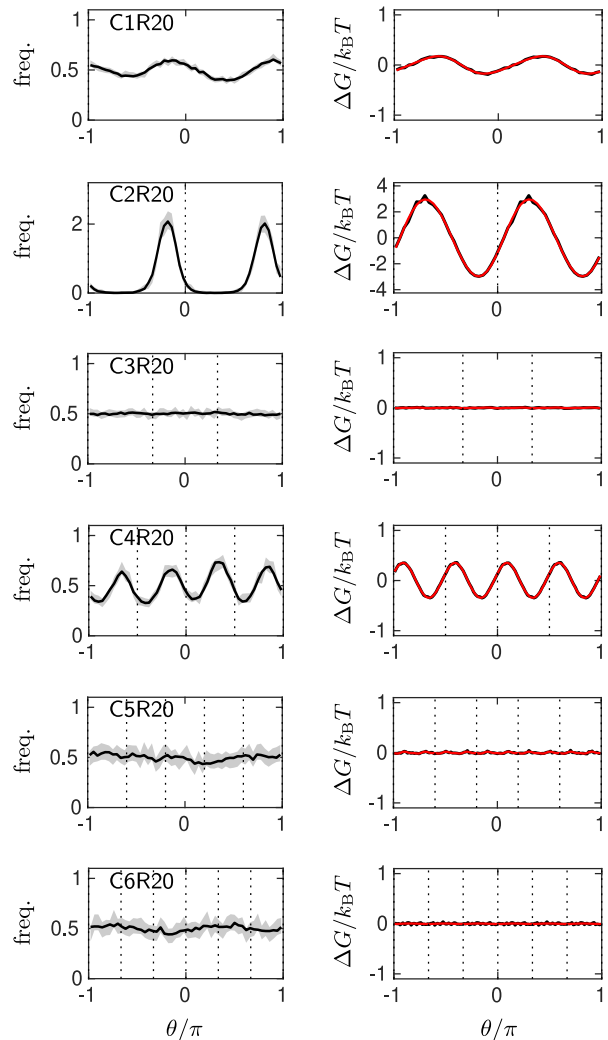


FIG. 3. Orientational distributions on cylinders. (Left) Orientational histograms of subunit one in 1- to 6-mers, with aggregated distributions (black) and 95% bootstrapped confidence intervals (gray). (Right) Corresponding orientational free energy, where the symmetries of the cylinder and protein structures have been imposed to improve the statistics. Solid black lines are averages, and red lines are least-square fits to Fourier series with two terms.

### Orientational distributions

First, we simulated proteins with 1- to 6-fold symmetry on cylinders with radii  $R = 20\sigma$ . The principal curvatures of a cylinder is zero in the longitudinal direction, and  $1/R$  in the circumferential direction, so the local curvature experienced by the protein varies with the orientation angle  $\theta$ . Fig. 3(left) shows orientational distributions of a single subunit of the different proteins, averaged over multiple replicas with different initial orientations (see Methods). Non-flat distributions indicate orientational curvature sensing, and are seen in monomers, dimers, and tetramers, with dimers showing the largest ampli-

tude by far. For 3-,5-, and 6-mers we see no orientational preferences within our sampling accuracy.

The number of peaks reflect two symmetries of our setup: the cyclic symmetry of the proteins, and invariance under rotation of the whole system around an axis in the  $(x, y)$ -plane, which turns it upside down ( $\theta \rightarrow \theta + \pi$ ). By including all subunits and enforcing the upside down symmetry to further improve sampling, we construct the orientational free energy profiles shown in Fig. 3 (right).

### Elastic theory

Why do only monomers, dimers, and tetramers sense anisotropic curvature? A simple model can explain this behavior, if we assume that the curvature-dependent binding free energy of a protein depends on the local curvature [11–17]. The curvature tensor is given by

$$h = \begin{bmatrix} h_{\parallel} & h_X \\ h_X & h_{\perp} \end{bmatrix} = \begin{bmatrix} H + D \cos 2\theta & D \sin 2\theta \\ D \sin 2\theta & H - D \cos 2\theta \end{bmatrix}, \quad (1)$$

in a basis where  $\hat{e}_{\parallel}$  follows the protein orientation and is rotated by  $\theta$  w.r.t. the principal curvature direction  $\hat{e}_1$ . We have introduced the mean and deviatoric curvatures

$$H = (c_1 + c_2)/2, \quad D = (c_1 - c_2)/2, \quad (2)$$

with  $c_{1,2}$  being the principal curvatures. The Gaussian curvature is  $K = c_1 c_2 = 4(H^2 - D^2)$ . With  $\hat{e}_1 = \hat{e}_z$  as illustrated in Fig. 2b, the principal curvatures are  $c_1 = 0$  and  $c_2 = 1/R$ . In general,  $c_{1,2}$ , as well as the reference direction for  $\theta$ , may vary with the protein position. We also note that the curvature tensor is invariant under half turn rotations,  $\theta \rightarrow \theta + \pi$ , just as the cylinder geometry. In our model, the curvature-dependent part of the binding free energy per molecule,  $G$ , is a function of the local curvature,  $G = G(\vec{x}, \theta) = \hat{G}(h(\vec{x}, \theta))$ , that can be expanded in a Taylor series in  $h_1 = \frac{1}{2}(h_{\parallel} + h_{\perp}) = H$ ,  $h_2 = \frac{1}{2}(h_{\parallel} - h_{\perp}) = D \cos(2\theta)$ , and  $h_3 = h_X = D \sin(2\theta)$ ,

$$G = \sum_i \alpha_i^{(1)} h_i + \sum_{ij} \alpha_{ij}^{(2)} h_i h_j + \dots, \quad (3)$$

where  $\alpha_{i,j,\dots}^{(m)}$  are coefficients for terms of order  $m$  in curvature. The lowest-order constant term is irrelevant and has been discarded. In general, there are  $(m+1)(m/2+1)$  terms of order  $m$  [20], but symmetry can impose restrictions on the coefficients. For example, combinations such as  $h_{\parallel} + h_{\perp} = 2H$  and  $h_{\parallel} h_{\perp} - h_X^2 = K$  are invariant under rotations and compatible with all structural symmetries. To see how symmetry restricts the curvature dependence, we rewrite Eq. (3) as a Fourier series,

$$G = a_0 + \sum_{n=1}^{\infty} [a_{2n} \sin(2n\theta) + b_{2n} \cos(2n\theta)], \quad (4)$$

where the  $a, b$  coefficients are functions of  $H, D$  (or  $H, K$ ), but independent of  $\theta$ . The fact that the curvature

tensor elements in Eq. (3) depend on  $\theta$  only through  $h_2 = D \cos(2\theta)$  and  $h_3 = D \sin(2\theta)$  means that only even multiples of  $\theta$  are included in Eq. (4), and that higher order Fourier terms are also higher order in curvature. To see this, we note that translating between the Fourier and Taylor series expansions involves the use of trigonometric addition formulae [21], which in this setting reads

$$D^n \sin(2n\theta) = \sum_{k=0}^n \sin\left[\frac{\pi}{2}(n-k)\right] \binom{n}{k} h_2^k h_3^{n-k}, \quad (5)$$

$$D^n \cos(2n\theta) = \sum_{k=0}^n \cos\left[\frac{\pi}{2}(n-k)\right] \binom{n}{k} h_2^k h_3^{n-k}. \quad (6)$$

It follows that the lowest-order curvature dependence in the coefficients of  $\sin(2n\theta)$  and  $\cos(2n\theta)$  is  $D^n$ . Moreover, the binding free energy of a protein with  $M$ -fold cyclic symmetry is invariant under rotations of  $1/M$  turns, i.e.,

$$G(\vec{x}, \theta) = G\left(\vec{x}, \theta + \frac{2\pi}{M}\right), \quad (7)$$

which is only true for those terms in Eq. (4) where  $2n$  is a multiple of  $M$ . This leaves monomers and dimers ( $M = 1, 2$ ) unrestricted, but for  $M = 3, 4, 5, 6$  the lowest non-zero Fourier terms are  $2n = 6, 4, 10, 6$ , which are of order  $D^3, D^2, D^5, D^3$ , respectively. These are the leading-order contributions to the orientational free energy amplitudes in Fig. 3, which suggests a simple explanation for the amplitude pattern: non-zero linear and quadratic terms are needed to produce an angular dependence, while the effects of higher order terms are too small to see. The pattern continues for higher symmetries. For even  $M$ -mers, the lowest order anisotropic terms are  $D^{M/2} \cos(M\theta)$ ,  $D^{M/2} \sin(M\theta)$ , while for odd  $M$ -mers, the lowest order terms are  $D^M \cos(2M\theta)$ ,  $D^M \sin(2M\theta)$ . Monomers, dimers, and tetramers are therefore the only symmetries with significant anisotropic curvature sensing at moderate curvatures. For example, the lowest order anisotropic terms compatible with tetramers are  $D^2 \sin(4\theta) = h_x(h_{\parallel} - h_{\perp})$  and  $D^2 \cos(4\theta) = \frac{1}{4}(h_{\parallel} - h_{\perp})^2 - h_X^2$ .

The above theory makes testable predictions. First, higher order terms should become prominent at high enough curvatures. In particular,  $D^3 \sin(6\theta)$ ,  $D^3 \cos(6\theta)$  should produce orientational distributions with 6-fold periodicity for a trimer at high enough curvature. This is clearly demonstrated when the cylinder radius is decreased from  $20\sigma$  to  $7\sigma$  in Fig. 4a.

Second, different symmetries should produce different relationships between the deviatoric curvature  $D$  and the amplitude of the rotational free energy, depending on the order of the lowest order terms. Since the magnitude of  $D$  is proportional to  $1/R$  on a cylinder, the tetramer amplitude should scale as  $1/R^2$ , while the trimer amplitude should scale as  $1/R^3$ . Monomers and dimers allow anisotropic terms that are both linear and quadratic in  $D$ , which implies a scaling relation involving both  $1/R$  and  $1/R^2$ . (All amplitudes tend to zero at vanishing curvature.) We simulated monomers, trimers, and tetramers

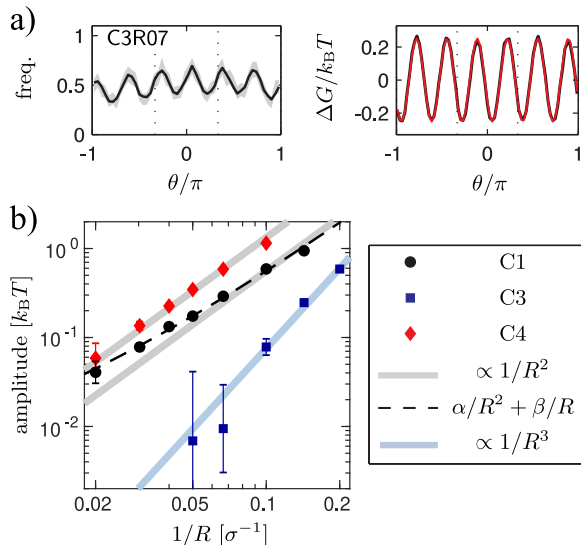


FIG. 4. a) Rotational distribution and free energy of a trimer at high curvature ( $R = 7\sigma$ ), computed as in Fig. 3. b) Rotational free energy amplitudes vs  $1/R$ . The monomer protein (C1) amplitude is well described by a phenomenological fit to a general quadratic relation,  $\alpha/R^2 + \beta/R$ . The trimer (C3) and tetramer (C4) show the expected scaling as  $1/R^3$  and  $1/R^2$ , respectively. Error bars are 95% confidence intervals, estimated by bootstrapping (see Supplementary Methods).

on a range of cylinder radii. Fig. 4b shows the resulting amplitudes plotted against  $1/R$ . The results are in good agreement with the theory: The predicted quadratic and cubic scalings for the tetramer and trimer are clearly visible, while the monomer amplitude approaches zero slower than  $1/R^2$  for increasing  $R$ , as expected.

## Discussion

Our simulations and theoretical analysis classify membrane proteins in two categories of curvature sensing behavior depending on their structural symmetry: Monomers and homo-multimeric dimers and tetramers are allowed by symmetry to sense curvature anisotropically, meaning that direction dependent terms of first or second order are allowed in the binding free energy. Trimers, pentamers and higher order symmetric proteins couple to curvature isotropically, meaning that only direction-independent low-order terms are allowed. Our analysis also suggests that dimers are the strongest anisotropic curvature sensors, as in Fig. 3. The 2-fold symmetry of the curvature tensor allows dimeric subunits to amplify each other constructively, while subunits in proteins with higher symmetry partly counteract each

other by canceling out low order terms.

These results have biological implications. Anisotropic curvature sensing could be useful for some protein functions, but not others, which implies a correlation between structural symmetry and the biological function of membrane proteins. Proteins that stabilize, localize to, and/or function on, anisotropically curved membrane structures such as ridges, tubes, and pores, could be expected to sense anisotropic curvature, and hence be found as monomers, dimers, or tetramers. BAR domain proteins, that stabilize membrane tubules [7, 22] for example during endocytosis [23], are indeed dimers. The (hetero-multimeric) functional units of the rotary motor protein  $F_1F_o$  (ATP synthase) can dimerize in order to assemble along, and stabilize, the highly curved ridges of mitochondrial inner membranes [24]. The M2 proton channel, which mediates virus budding and localizes to the neck of budding virions [25], is a tetramer. In addition to localization and stabilization of anisotropic membrane structures, anisotropic curvature sensing also allows the membrane shape to organize the in-plane orientation of proteins. This could facilitate the formation of regular protein coats, for example by BAR domains bound to membrane tubules at high density [26]. On the other hand, membrane proteins that do not need to sense anisotropic curvature may profit from being structurally prohibited to do so. One example might be ion channels gated by membrane tension, which is an isotropic mechanical signal. Notable members of this class are the mechanosensitive channels of large (MscL, pentamer [27]) and small (MscS, heptamer [28]) conductance, and the trimeric ion channel Piezo1 [29]. Beyond these examples, bioinformatic methods may be able to probe correlations between biological function and structural symmetry in membrane proteins more systematically.

Experimentally, anisotropic curvature sensors are difficult to characterize microscopically because of the larger number of possible terms in the binding free energy. Explicit measurement of the in-plane orientation would be useful [11], for example using electron microscopy [24] or polarized light [30]. Finally, the present study is limited to sensing pure curvature, and it might be interesting to extend this analysis to consider curvature gradients as well, since they have different symmetry properties [19].

*Acknowledgments.* This work was supported by the Swedish Research Council (Vetenskapsrådet, grant 2017-03950 to A.L.), Horizon 2020 programme (project Smart-NanoTox, to A.L. and E.G.B), the Wenner-Gren foundation and the Center for Biomembrane Research (to M.L.). The simulations were performed on resources provided by the Swedish National Infrastructure for Computing (SNIC) at HPC2N (Umeå University), NSC (Linköping University) and PDC (KTH Royal Institute of Technology).

[1] Yoko Shibata, Junjie Hu, Michael M. Kozlov, and Tom A. Rapoport, “Mechanisms shaping the membranes

of cellular organelles,” *Annu. Rev. Cell Dev. Biol.* **25**,

- 329–354 (2009).
- [2] Harvey T. McMahon and Jennifer L. Gallop, “Membrane curvature and mechanisms of dynamic cell membrane remodelling,” *Nature* **438**, 590–596 (2005).
  - [3] Tobias Baumgart, Benjamin R. Capraro, Chen Zhu, and Sovan L. Das, “Thermodynamics and mechanics of membrane curvature generation and sensing by proteins and lipids,” *Annu. Rev. Phys. Chem.* **62**, 483–506 (2011).
  - [4] Asger Tonnesen, Sune M Christensen, Vadym Tkach, and Dimitrios Stamou, “Geometrical membrane curvature as an allosteric regulator of membrane protein structure and function,” *Biophys. J.* **106**, 201–209 (2014).
  - [5] Marijn G. J. Ford, Ian G. Mills, Brian J. Peter, Yvonne Vallis, Gerrit J. K. Praefcke, Philip R. Evans, and Harvey T. McMahon, “Curvature of clathrin-coated pits driven by epsin,” *Nature* **419**, 361–366 (2002).
  - [6] Haosheng Cui, Edward Lyman, and Gregory A. Voth, “Mechanism of membrane curvature sensing by amphipathic helix containing proteins,” *Biophys. J.* **100**, 1271–1279 (2011).
  - [7] Brian J Peter, Helen M Kent, Ian G Mills, Yvonne Vallis, P Jonathan G Butler, Philip R Evans, and Harvey T McMahon, “Bar domains as sensors of membrane curvature: the amphiphysin bar structure,” *Science* **303**, 495–499 (2004).
  - [8] Sophie Aimon, Andrew Callan-Jones, Alice Berthaud, Mathieu Pinot, Gilman ES Toombes, and Patricia Bassereau, “Membrane shape modulates transmembrane protein distribution,” *Dev. Cell* **28**, 212–218 (2014).
  - [9] David S. Goodsell and Arthur J. Olson, “Structural symmetry and protein function,” *Annu. Rev. Biophys. Biomol. Struct.* **29**, 105–153 (2000).
  - [10] Ira R Cooke and Markus Deserno, “Solvent-free model for self-assembling fluid bilayer membranes: stabilization of the fluid phase based on broad attractive tail potentials,” *J. Chem. Phys.* **123**, 224710 (2005).
  - [11] Jordi Gómez-Llobregat, Federico Elías-Wolff, and Martin Lindén, “Anisotropic membrane curvature sensing by amphipathic peptides,” *Biophys. J.* **110**, 197–204 (2016).
  - [12] N. Ramakrishnan, P.B. Sunil Kumar, and Ravi Radhakrishnan, “Mesoscale computational studies of membrane bilayer remodeling by curvature-inducing proteins,” *Physics Reports* **543**, 1–60 (2014).
  - [13] N. Ramakrishnan, P. B. Sunil Kumar, and John H. Ipsen, “Membrane-mediated aggregation of curvature-inducing nematogens and membrane tubulation,” *Biophys. J.* **104**, 1018–1028 (2013).
  - [14] Kiyotaka Akabori and Christian D. Santangelo, “Membrane morphology induced by anisotropic proteins,” *Phys. Rev. E* **84**, 061909 (2011).
  - [15] Šárka Perutková, Veronika Kralj-Iglič, Mojča Frank, and Ales Iglič, “Mechanical stability of membrane nanotubular protrusions influenced by attachment of flexible rod-like proteins,” *J Biomech* **43**, 1612–1617 (2010).
  - [16] J. B. Fournier, “Nontopological saddle-splay and curvature instabilities from anisotropic membrane inclusions,” *Phys. Rev. Lett.* **76**, 4436–4439 (1996).
  - [17] S. Leibler, “Curvature instability in membranes,” *J. Phys.-Paris* **47**, 10 (1986).
  - [18] Ira Cooke, Kurt Kremer, and Markus Deserno, “Tunable generic model for fluid bilayer membranes,” *Phys. Rev. E* **72**, 011506 (2005).
  - [19] Federico Elías-Wolff, Martin Lindén, Alexander P. Lyubartsev, and Erik G. Brandt, “Computing curvature sensitivity of biomolecules in membranes by simulated buckling,” *Journal of Chemical Theory and Computation* **14**, 1643–1655 (2018).
  - [20] Each term of order  $m$  in Eq. (3) can be written on the form  $h_1^i h_2^{j-i} h_3^{m-j}$ , with  $0 \leq i \leq j \leq m$ . The number of distinct terms therefore equals the number of  $i, j$ -combinations, given by  $\sum_{i=0}^m \sum_{j=i}^m 1 = (m+1)\binom{m}{2} + 1$ .
  - [21] Eric W. Weisstein, “Multiple-Angle Formulas.” From MathWorld—A Wolfram Web Resource., <http://mathworld.wolfram.com/Multiple-AngleFormulas.html>.
  - [22] Adam Frost, Vinzenz M. Unger, and Pietro De Camilli, “The BAR domain superfamily,” *Cell* **137**, 191–196 (2009).
  - [23] Jian Liu, Yidi Sun, David G. Drubin, and George F. Oster, “The mechanochemistry of endocytosis,” *PLoS Biol.* **7**, e1000204 (2009).
  - [24] Karen M. Davies, Claudio Anselmi, Ilka Wittig, José D. Faraldo-Gómez, and Werner Kühlbrandt, “Structure of the yeast F1Fo-ATP synthase dimer and its role in shaping the mitochondrial cristae,” *Proc. Natl. Acad. Sci. U.S.A.* **19**, 13602–13607 (2012).
  - [25] Jeremy S Rossman, Xianghong Jing, George P Leser, and Robert A Lamb, “Influenza virus M2 protein mediates ESCRT-independent membrane scission,” *Cell* **142**, 902–913 (2010).
  - [26] Adam Frost, Rushika Perera, Aurélien Roux, Krasimir Spasov, Olivier Destaing, Edward H. Egelman, Pietro De Camilli, and Vinzenz M. Unger, “Structural basis of membrane invagination by F-BAR domains,” *Cell* **132**, 807–817 (2008).
  - [27] Geoffrey Chang, Robert H. Spencer, Allen T. Lee, Margaret T. Barclay, and Douglas C. Rees, “Structure of the MscL homolog from *Mycobacterium tuberculosis*: A gated mechanosensitive ion channel,” *Science* **282**, 2220–2226 (1998).
  - [28] R. B. Bass, “Crystal structure of *Escherichia coli* MscS, a voltage-modulated and mechanosensitive channel,” *Science* **298**, 1582–1587 (2002).
  - [29] Yusong R. Guo and Roderick MacKinnon, “Structure-based membrane dome mechanism for Piezo mechanosensitivity,” *eLife Sciences* **6**, e33660 (2017).
  - [30] Stephanie A. Rosenberg, Margot E. Quinlan, Joseph N. Forkey, and Yale E. Goldman, “Rotational motions of macromolecules by single-molecule fluorescence microscopy,” *Acc. Chem. Res.* **38**, 583–593 (2005).
  - [31] [github.com/kaplajon/mxdrfile](https://github.com/kaplajon/mxdrfile).
  - [32] Vagelis A. Harmandaris and Markus Deserno, “A novel method for measuring the bending rigidity of model lipid membranes by simulating tethers,” *J. Chem. Phys.* **125**, 204905 (2006).

## Appendix A: Supplementary methods

*a. Coarse-grained lipid model.* We used the Cooke *et al.* [18] lipid model in our simulations. Lipid molecules are represented by one head- and two tail beads (see Fig. 1). The solvent is modeled implicitly, and lipid bilayers are stabilized by long-range attractive interactions between tail beads. The model is expressed in terms of the three scales  $\sigma$  (length),  $\epsilon$  (energy), and  $\tau$  (time). As in our previous work [19], we choose tuning parameters  $w_c = 1.6\sigma$  (decay length of tail attraction) and temperature  $k_B T = 1.08\epsilon$ , to yield stable bilayers in the fluid phase [18]. Simulations were carried out with Gromacs 2016.3, 2016.5, and 2018.1, at constant volume, using a leap-frog stochastic dynamics integrator with time step  $0.01\tau$  and friction constant  $\Gamma = \tau^{-1}$ . Under these conditions, comparisons of lipid bilayer thickness and lipid diffusion indicate  $\sigma \approx 1$  nm and  $\tau \approx 10$  ns [10]. Coordinates were saved every  $500\tau$ .

We constructed protein models by assembling an asymmetric transmembrane monomer comprised of 54 tail-beads sandwiched between two layers of 9 head beads (Fig. 1c). The monomer was given a wedged cross-section by compressing the beads on one side, corresponding to curvature radii of  $5\sigma$  and  $25\sigma$ , in the transverse and longitudinal directions, respectively. We then formed multimeric protein structures by combining monomers rotated around the membrane normal (Fig. 1d-g), and stabilized the resulting structures by elastic springs of strength  $100\epsilon/\sigma^2$  between all beads closer than  $4\sigma$ . We have previously studied the trimer in this family, and found a preferred curvature of about  $0.035\sigma^{-1}$  [19]. We used custom Matlab scripts based on the mxdrfile package [31] to construct the elastic network models, generate initial configurations, and to analyze data sets.

*b. Simulating curvature sensing on cylinders.* For curvature sensing simulations, we assembled cylindrical bilayers with a mid-monolayer density close to that of a flat bilayer. A protein molecule was inserted in the bilayer and clashing lipids were removed. We assembled multiple replicas for every combination of multimer and cylinder size, distinguished by different initial protein in-plane orientation and by small random long-wavelength perturbations to all particles. After energy minimization and a burn-in simulation of  $10^3\tau$ , we ran production runs for  $10^6\tau$  or  $2 \times 10^6\tau$ , saving positions every  $500\tau$ . Relaxation of cylindrical systems is facilitated by the artificially high flip-flop rate of the Cooke model [32]. System size parameters and the number of production runs are summarized in Table S1.

*c. Data analysis.* At every sample point, we computed the in-plane orientation by least-square fitting straight lines through a selected set of core particles in each monomer. The line was projected on the cylinder tangent plane intersecting the protein midpoint, and the

in-plane orientation of that subunit was computed as the angle between the projected line and the  $z$ -axis.

Only data from subunit one is included in orientation angle histograms (e.g., Fig. 3, left). For analyzing the free energy profiles and their amplitudes (Fig. 3, right), we included the in-plane orientation of all subunits, as well as replicas rotated by  $\pi$ , to enforce the 2-fold rotation symmetry of the curvature tensor itself. (That is,  $2m$  values from each configuration of an  $m$ -mer.) We then aggregated data from all simulations of each system size into a single histogram with number of bins proportional to the protein multiplicity, and computed the free energy as the negative log density. To compute the amplitude of the resulting free energy profile, we first fitted a truncated Fourier series with the two lowest wave-lengths, and then extracted the amplitude of the fit. Examples of such fits are shown in red in Fig. 3(right), displaying excellent agreement. Error bars in Figs. 3 and 4 correspond to 95% bootstrapped confidence intervals from  $10^4$  bootstrap realizations. These were computed from the aggregated data, taking only uncorrelated data points (auto-correlation times range from  $1200\tau$  for the monomer, to  $8000\tau$  for the dimer). The error bars in Fig. 4b correspond to relative errors, that is, for a given amplitude  $y$  with bootstrap confidence intervals  $\pm\delta y$  in linear space, the relative error in logarithmic scale, where  $z = \log_{10} y$ , corresponds to  $\delta z = (\log 10)^{-1} \delta y / y$ .

name	$M$	$R[\sigma]$	$H[\sigma]$	$N_{\text{lip}}$	$N_{1M}$	$N_{2M}$
C1R07	1	7	60	4550	-	32
C1R10	1	10	60	6520	-	27
C1R15	1	15	75	12290	83	17
C1R20	1	20	75	16420	75	25
C1R25	1	25	75	20480	75	25
C1R33	1	33	75	27060	25	75
C1R50	1	50	75	41060	-	34
C2R20	2	20	75	16395	25	-
C3R05	3	5	60	3225	-	25
C3R07	3	7	60	4515	-	25
C3R10	3	10	60	6475	-	44
C3R15	3	15	75	12240	-	100
C3R20	3	20	75	16370	-	100
C4R10	4	10	60	6460	-	50
C4R15	4	15	75	12230	-	54
C4R20	4	20	75	16355	-	55
C4R25	4	25	75	20420	-	54
C4R33	4	33	75	27000	-	62
C4R50	4	50	75	41000	-	26
C5R20	5	20	75	16345	-	25
C6R20	6	20	75	16330	-	25

TABLE S1. Summary of production runs.  $M$ : number of protein subunits,  $R$ : cylinder radius,  $H$ : cylinder height,  $N_{\text{lip}}$ : approximate number of lipids (varies by less than  $\pm 20$  between same name replicas),  $N_{1M}$ : number of  $10^6\tau$  production runs,  $N_{2M}$ : number of  $2 \times 10^6\tau$  production runs.